Journal of Nuclear Materials 433 (2013) 132–142

Contents lists available at SciVerse ScienceDirect

Journal of Nuclear Materials

journal homepage: www.elsevier.com/locate/jnucmat

Impact of thermal conductivity models on the coupling of heat transport, oxygen diffusion, and deformation in (U, Pu)O_{2-x} nuclear fuel elements

Bogdan Mihaila [a,*], Marius Stan [b], Justin Crapps [a], Di Yun [b]

[a] Materials Science and Technology Division, Los Alamos National Laboratory, Los Alamos, NM 87545, USA
[b] Nuclear Engineering Division, Argonne National Laboratory, Argonne, IL 60439, USA

ARTICLE INFO

Article history:
Received 27 July 2012
Accepted 7 September 2012
Available online 16 September 2012

ABSTRACT

We study the coupled thermal transport, oxygen diffusion, and thermal expansion in a generic nuclear fuel rod consisting of a $(U_{1-y}Pu_y)O_{2-x}$ fuel pellet separated by a helium gap from zircaloy cladding. Steady-state and time-dependent finite-element simulations with a variety of initial- and boundary-value conditions are used to study the effect of the Pu content, y, and deviation from stoichiometry, x, on the temperature and deformation profiles in this fuel element. We find that the equilibrium radial temperature and deformation profiles are most sensitive to x at small values of y. For larger values of y, the effects of oxygen and Pu content are equally important. Following a change in the heat-generation rate, the centerline temperature, the radial deformation of the fuel pellet, and the centerline deviation from stoichiometry track each other closely in $(U, Pu)O_{2-x}$, as the characteristic time scales of the heat transport and oxygen diffusion are similar. This result is different from the situation observed in the case of UO_{2+x} fuels.

© 2012 Elsevier B.V. All rights reserved.

1. Introduction

Homogeneous mixed oxide (U, Pu)O_{2-x} fuels are used in existing nuclear reactors as part of a strategy intended to address the issue of large stockpiles of plutonium accumulated around the word from dismantled nuclear weapons and reprocessing of nuclear fuels [1]. This type of fuel is also of interest for the IVth generation nuclear reactors, especially at high Pu concentrations, due to the potential for decreasing the amount of minor actinides in high level radioactive waste and the improved proliferation resistance [2]. Although at low Pu content, the thermal, chemical, and mechanical properties of MOX fuels are similar to the properties of UO_2 fuels, the thermal conductivity of the MOX fuel is slightly lower which may lead to a slower rate of heat removal from the fuel pellet and a higher center line fuel temperature. This aspect was examined using in-pile experimental results and fuel performance codes for the case of pressurized water reactors (PWRs) [3].

Because fuel performance simulations often make assumptions that are consistent with thermo-mechanical and chemical equilibrium, the thermodynamics of the U–Pu–O system is the subject of computational studies aimed at verifying the self-consistency of the calculations without significantly impeding computational performance [4]. The thermodynamic properties and phase diagram of the U–Pu–O system have been assessed using experimental and computational methods and the results stored in databases covering a wide range of composition and temperatures [5]. The results show that the oxygen potential and equilibrium oxygen content in U–Pu–O fuels is controlled by the change of oxidation state of the cations (U and Pu) with temperature. The thermal conductivity of U–Pu oxides was examined using experimental methods, such as laser flash for the oxide (U, Pu)O_{2-x} and for solid solutions that involve minor actinides, such as (U, Pu, Np)O_2 and (U, Pu, Am)O_2 solid solutions. It was determined that the effect of the Np content is much smaller that the effect of the Am content [6,7]. The thermal conductivity of the mixed oxides is sensitive to the Pu content but is much more dependent on the oxygen content. Laser flash studies of the influence of the oxygen potential on the thermal conductivity of the mixed (U, Pu)O_{2-x} demonstrate that the most critical factors are the temperature and the oxygen content [8].

Understanding the main mechanisms of radiation damage and predicting the evolution of fuel properties in the reactor are major challenges of fuel performance codes [9,10]. In addition to the complex chemistry and evolving microstructure of the materials (ceramic fuel pellet or metallic fuel rod, and metallic cladding), several phenomena compete in determining the performance of the fuel element. Among them, heat transport, chemical transport of oxygen and fission products, and pellet and clad thermal expansion play critical roles. Recent studies demonstrate that these phenomena are closely coupled and that including the coupling in computer simulations provides insight into the characteristic response of the fuel element to rapid changes in the operating conditions that cannot be acquired via qualitative estimations [9,10]. For

* Corresponding author.
E-mail address: bmihaila@lanl.gov (B. Mihaila).

0022-3115/$ - see front matter © 2012 Elsevier B.V. All rights reserved.
http://dx.doi.org/10.1016/j.jnucmat.2012.09.017

example, in UO_{2+x} fuels, due to widely varying Lewis numbers, the temperature and deformation of the fuel rapidly respond to power excursions (minutes and hours) while the oxygen content (e.g. non-stoichiometry, x) reaches steady state values after days or even weeks [11,12]. Moreover, fuel and clad materials properties such as density, specific heat, and thermal conductivity change with temperature and composition, especially oxygen content. Coupled simulations of heat transport, oxygen diffusion and deformation of UO_{2+x} fuel elements with metallic cladding show that accounting for oxygen content in the thermal conductivity model, $k(T,x)$, leads to predictions of centerline temperature values that are substantially different (100–200 K) from the predictions performed using composition-independent models, $k(T)$ [11,12]. It is therefore important to use material property models that include both temperature and chemical composition, especially oxygen content (non-stoichiometry, x).

Choosing a good model for the thermal conductivity of the oxide fuel is very important. We have recently studied the impact of the thermal conductivity model on the coupled thermal transport, oxygen diffusion, and thermal expansion of a generic nuclear fuel element consisting of a UO_{2+x} fuel pellet and stainless steel cladding separated by a helium gap [13]. The thermo-mechanical response of the fuel element was evaluated using a series of steady-state and time-dependent finite-element simulations with a variety of initial- and boundary-value conditions. The results show that models that simulations that include the deviation from stoichiometry, x, in the thermal conductivity model lead to more accurate predictions of the centerline temperature and the radial deformation of the fuel pellet.

In this work we expand upon our previous studies [11–13] and investigate the impact of thermal conductivity models on the coupled thermal transport, oxygen diffusion, and thermal expansion simulation in (U, Pu)O_{2-x} fuel element with metallic cladding. The goal of the study remains the understanding of the sensitivity of the fuel performance simulations to various parameters, in particular to quality of the material models, and the coupling between different physics. To that end, we maintain the "generic" fuel-element geometry boundary conditions used in previous studies. However, to increase the relevance of the results to MOX fuel elements employed in PWR reactors, we use zircaloy cladding.

2. Multi-physics model

We consider a schematic model representation of a MOX fuel element, consisting of a fuel pellet separated by a helium gap from a zircaloy cladding (see Fig. 1). We chose a cylindrical fuel rod of radius $R_{\text{fuel}} = 4.3$ mm, a 0.03 mm width helium gap, and a cladding thickness of 0.5 mm.

The geometry of the fuel element is shown in Fig. 1. In this geometry we solve the coupled heat transport, oxygen diffusion and thermal expansion problem corresponding to a uniformly distributed source term, Q. The heat transport equation is given by

$$\rho C_P \frac{\partial T}{\partial t} = \nabla \cdot (k \cdot \nabla T) + Q, \tag{2.1}$$

where ρ, C_P and k are the density, specific heat at constant pressure and thermal conductivity, respectively. Because the MOX nuclear fuel is non-stoichiometric, all material properties of the fuel are dependent on both the temperature, T, and the deviation from stoichiometry, x,

$$x = |O/M - 2|, \tag{2.2}$$

where O/M denotes the oxygen-to-metal ratio.

To model the oxygen transport in MOX fuel elements, we assume without loss of generality, that hyper-stoichiometric (hypo-stoichiometric) systems are pseudo-binary systems described as

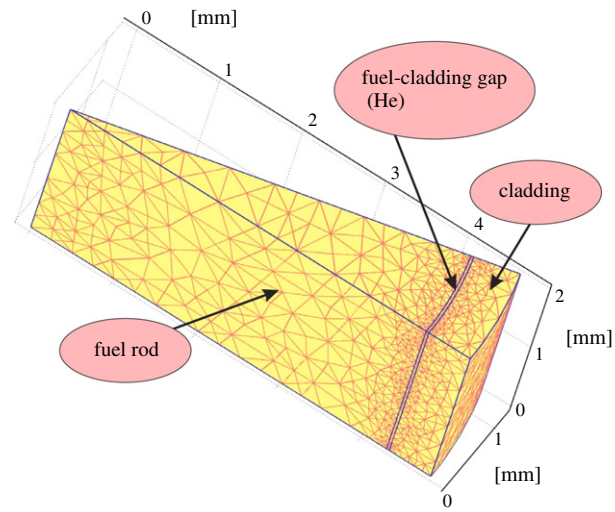

Fig. 1. Geometry of the fuel element.

dilute solutions of oxygen interstitials (vacancies) in the oxygen sublattice [14]. For hypo-stoichiometric fuel elements, we consider the continuity equation,

$$n \frac{\partial c}{\partial t} = \nabla \cdot \mathbf{J}, \tag{2.3}$$

where c denotes the atomic fraction of vacancies, $\mathbf{J}$ is the flux of oxygen vacancies, and n is the total number of regular oxygen sites per unit volume. Based on thermodynamic considerations [15], the flux of oxygen vacancies can be written as

$$\mathbf{J} = -nD\left[\nabla c + \frac{c(1-c)}{F}\frac{Q^*}{RT^2}\nabla T\right], \tag{2.4}$$

where D is the chemical diffusion coefficient, Q^* is the heat of transport, F is the thermodynamic factor, and R is the ideal gas constant. In Eq. (2.4), the gradient of non-stoichiometry is associated with the conventional Fickian diffusion contribution, whereas the term involving a gradient in temperature represents the thermal segregation or the Soret effect [16]. In the dilute limit, $x \to 0$, the thermodynamic factor has the limit $F \to 1$.

For hypo-stoichiometric oxides, MO_{2-x}, the atomic fraction of vacancies, c, is related to the deviation from stoichiometry, x, as

$$x = 2c. \tag{2.5}$$

Therefore, for MO_{2-x}, Eqs. (2.3) and (2.4) can be written only in terms of the deviation from stoichiometry, x, as

$$n \frac{\partial x}{\partial t} = \nabla \cdot \mathbf{J}, \tag{2.6}$$

with

$$\mathbf{J} = -nD\left[\nabla x + \frac{x(1+\frac{1}{2}x)}{F}\frac{Q^*}{RT^2}\nabla T\right]. \tag{2.7}$$

In the limit of very small deviations from stoichiometry, $x \ll 1$, Eq. (2.7) becomes

$$\mathbf{J} = -nD\left(\nabla x + \frac{x}{F}\frac{Q^*}{RT^2}\nabla T\right). \tag{2.8}$$

This is the same as the interstitial flux in hyper-stoichiometric metal oxides, MO_{2+x}.

The distributions of temperature and compositions are used to calculate the mechanical deformation of the pellet and cladding. In this model, the pellet and cladding are considered as uniform, pure elastic materials, characterized by the Young's modulus, E,

Poisson ratio, ν, thermal expansion coefficient, α, and density, ρ. The model accounts for the temperature and composition dependence of the mechanical properties. The fuel pellet and zircaloy cladding are allowed to expand freely.

The total strain tensor, ε, is written in terms of the gradient of the displacement, $\mathbf{u}$, as

$$\varepsilon = \frac{1}{2}\left(\nabla\mathbf{u} + \nabla\mathbf{u}^T\right). \tag{2.9}$$

The relationship between the stress tensor, σ, the strain tensor, ε, and temperature, T, is given by the Duhamel-Hooke's law, as

$$\sigma = \sigma_0 + C\cdot[\varepsilon - \varepsilon_0 - \alpha(T - T_{\mathrm{ref}})], \tag{2.10}$$

where C is the elasticity tensor, σ_0 and ε_0 are the initial stresses and strains, and T_{ref} is the reference temperature. The elasticity tensor, C, is given in terms of the Young's modulus, E, the Poisson ratio, ν, and the thermal expansion coefficient, α, as described for instance in Ref. [17].

The coupled system of Eqs. 2.1, 2.3, 2.8, 2.9 and 2.10 is solved self-consistently using a fully-coupled direct solver in Comsol Multiphysics. The calculations provide the evolution of the spatial distributions of temperature, T, deviation from stoichiometry, x, and deformation in the fuel element.

3. Material properties

Properties of the materials in the fuel element were obtained from previously published correlations and are summarized in Tables 1 and 2, for helium and the cladding material, respectively, and in Tables 3 and 4 for UO_2 and (U, Pu)O_2, respectively. Because this study is general in nature, in this paper we use generic zircaloy cladding material properties [19].

The thermal conductivity of the oxide fuel is given usually as the sum of a lattice phonon contribution and a polaron ambipolar term, with the generic form

$$k(T,x) = \frac{1}{A(x) + C(x)t} + \frac{B}{t^{\gamma}}\exp(-F/t), \tag{3.1}$$

where $t = T(K)/1000$, and $A(x)$, $C(x)$, B, F, and γ are parameters obtained by fitting experimental thermal conductivity data. The dependence on the deviation from stoichiometry x is relevant only in the lattice part of the thermal conductivity [27]. The ambipolar term is designed to fit the high temperature data and shows no dependence on x [28]. Fig. 2 shows the temperature dependence of the thermal conductivity. The change in the thermal conductivity due to porosity is calculated by multiplying the conductivity of the solid by the Maxwell-Eucken function

$$f_{\kappa}(p) = \frac{1-p}{1+(\kappa-1)p}. \tag{3.2}$$

Here, p is the fractional porosity, with $p < 0.2$, and κ is a porosity shape factor. The material property database MATPRO recommends a value of the porosity shape factor of $\kappa = 1.5$ (spherical pores), whereas the commonly used value is $\kappa = 3$ [20]. The simulations discussed in this paper assume a 96.5% dense fuel pellet and we did not take into account the changes in the fuel density due to irradiation effects discussed for instance in Ref. [27].

The thermal conductivity models used in this paper are summarized in Table 5 and the temperature dependence of these models is illustrated in Fig. 2. In Fig. 2a, we compare the various thermal conductivity models for stoichiometric (U, Pu)O_2. We note that the models proposed by Carbajo et al. (C01) [25] and Duriez et al. (D00) [30] differ only in the high-temperature choice for the ambipolar term and are applicable for less than 15% Pu content. The P92 model proposed by Philipponeau [31] is applicable for 20% Pu content. The variability of the (U, Pu)O_2 thermal conductivity as a function of the Pu content, y, is illustrated in Fig. 2b using the A11 model proposed by Amaya and collaborators [29]. We note that the thermal conductivity values reported by Amaya et al. are generally higher at low temperatures than those reported by other models used in this paper. However, the A11 model is the only model available that continuously varies the Pu content from 0 to 30%. Finally, in Fig. 2c we emphasize the stoichiometry dependence of the thermal conductivity models for $(\mathrm{U,Pu})O_{2-x}$. We depict here the changes in the temperature dependence of the thermal conductivity as a function of the deviation from stoichiometry, x, as inferred from the C01 and P92 models. In the temperature range $T < 1500$ K relevant for our simulations, the models C01, D00 and P92 produce similar results. The MATPRO (II) model is independent of the Pu content, y, and the deviation from stoichiometry, x.

In our simulations, the heat capacity of $(U_{1-y}Pu_y)O_2$ is calculated using the Kropp-Neumann rule that assumes $UO_2 - PuO_2$ solution mixture. We have

$$C_P[(U_{1-y}Pu_y)O_2] = (1-y)\,C_P[UO_2] + y\,C_P[PuO_2]. \tag{3.3}$$

Similarly, for hypo-stoichiometric mixed-oxides systems, we have

$$C_P[(U_{1-y}Pu_y)O_{2-x}] = (1+x)\,C_P[(U_{1-y}Pu_y)O_2] - \frac{x}{2}\,C_P[O_2]. \tag{3.4}$$

In the following, we will use the heat capacity correlations recommended by Fink for UO_2 and PuO_2 [20,32], with the parameters given in Table 6. In Fig. 3a we illustrate the temperature dependence of these correlations, together with the corresponding MATPRO recommendations. In Fig. 3b we illustrate the variability of the (U, Pu)O_2 heat capacity temperature dependence as a function of the Pu content, y, calculated with Eq. (3.3) using the UO_2 and PuO_2 correlations recommended by Fink [20,32].

The density and thermal expansion coefficients used here follow the recommendations of Carbajo et al. who argue that UO_2, PuO_2, and $(U_{1-y}Pu_y)O_2$ exhibit similar thermal expansion behavior. Therefore, we use the equations developed by Martin [21] (see Tables 3 and 4), which also includes a weak dependence on x, the deviation from stoichiometry, in the case of hypo-stoichiometric (U, Pu)O_2. The room-temperature density is given by

$$\rho_{[273\mathrm{K}]} = 10{,}970 + 490y, \qquad (\mathrm{kg/m^3}), \tag{3.5}$$

with limiting cases the densities of uranium and plutonium oxides, 10,970 and 11,460 kg/m^3, respectively.

For the oxygen diffusion in UO_2 we chose the chemical diffusion coefficient recommended by Meachen [24], whereas for $(U_{1-y}Pu_y)O_2$ we use the correlation reported by Kato et al. [26]. The temperature dependence of these chemical diffusion coefficients is depicted in Fig. 4. We note that the Pu presence in the MOX fuel results in a significant increase in the oxygen mobility in the lattice. To complete the oxygen diffusion model in $(\mathrm{U,Pu})O_{2-x}$, we choose the heat of transport model given by Sari and Schumacher [14] and modified by Lassmann [23] that corresponds to a thermodynamic factor, $F = 1$. For consistency, the Soret diffusion parameters

Table 1
Summary of the properties of the helium filling the gap between the fuel pellet and the cladding (see Fig. 1). Here, ρ, C_P and k denote the density, heat capacity and thermal conductivity, respectively.

Property (material)	Functional form of the property on temperature, T	Units	Source
ρ [He]	$0.0818 - 8.275\times10^{-15}(T-600)$	kg/m^3	[18]
C_P [He]	5190	J/(kg K)	[18]
k [He]	$0.04679 + 3.81\times10^{-4}T - 6.786\times10^{-8}T^2$	W/(m K)	[18]

Table 2
Summary of the zircaloy cladding material properties. In addition to the notations introduced in Table 1, we use α_T, E and ν to denote the thermal expansion coefficient, the Young's elasticity module and Poisson ratio, respectively. At cladding temperatures relevant to the calculations discussed in this paper, the zircaloy is in the α phase, i.e. $T_{\text{clad}} < 1083$ K.

Property (material)	Functional form of the property on temperature, T	Units	Source
ρ [α zircaloy]	$6595.2 - 0.1477T$	kg/m^3	[19]
C_P [α zircaloy]	$255.66 + 0.1024T$	J/(kg K)	[19]
k [α zircaloy]	$11.498 + 4.6765 \times 10^{-3}\,T + 2.761 \times 10^{-6}\,T^2 + 2.2147 \times 10^{-9}\,T^3$	W/(m K)	[19]
α_T [α zircaloy]	$\begin{cases} 7.092 \times 10^{-6}, & \text{radial} \\ 9.999 \times 10^{-6}, & \text{angular} \\ 5.458 \times 10^{-6}, & \text{axial} \end{cases}$	m/(m K)	[19]
E [α zircaloy]	$108.8 \times 10^9 - 5.475 \times 10^7\,T$	Pa	[19]
ν [α zircaloy]	0.3		[19]

Table 3
Summary of UO_{2+x} material properties. In addition to the notations introduced in Tables 1 and 2, we introduce Q^*, F and D to denote the heat of transport, thermodynamic and chemical diffusion coefficient of oxygen in UO_2.

Property (material)	Functional form of the property on temperature, T, and non-stoichiometry, x	Units	Source
ρ [UO_2]	$10,970\,(a + bT + cT^2 + dT^3)^{-3}$, with $\left.\begin{matrix} a = 0.99734,\ b = 9.802 \times 10^{-6}, \\ c = -2.705 \times 10^{-10},\ d = 4.391 \times 10^{-13} \end{matrix}\right\}$, for $T \leqslant 923$ K, $\left.\begin{matrix} a = 0.99672,\ b = 1.179 \times 10^{-5}, \\ c = -2.429 \times 10^{-9},\ d = 1.219 \times 10^{-12} \end{matrix}\right\}$, for $T > 923K$.	kg/m^3	[20,21]
α_T [UO_2]	$a + bT + cT^2 + dT^3$, with $\left.\begin{matrix} a = 9.828 \times 10^{-6},\ b = -6.390 \times 10^{-10}, \\ c = 1.33 \times 10^{-12},\ d = -1.757 \times 10^{-17} \end{matrix}\right\}$, for $T \leqslant 923$ K, $\left.\begin{matrix} a = 1.1833 \times 10^{-5},\ b = -5.013 \times 10^{-9}, \\ c = 3.756 \times 10^{-12},\ d = -6.125 \times 10^{-17} \end{matrix}\right\}$, for $T > 923$ K.	m/(m K)	[20,21]
E [UO_{2+x}]	$2.334 \times 10^{11}\,(1 - 1.095 \times 10^{-4}\,T)\,\exp(-1.34x)$	Pa	[22]
ν [UO_2]	0.316		[22]
Q^* [UO_{2+x}]	$-1.02 \times 10^5 \exp(-34x)$	J/mol	[23,14]
F [UO_2]	1		[23,14]
D [UO_2]	$10^{-3.6-7.12\times10^3/T}$	m^2/s	[24]

Table 4
Summary of $(U_{1-y}Pu_y)O_{2-x}$ material properties. Notations follow the same conventions as before.

Property (material)	Functional form of the property on temperature, T, and non-stoichiometry, x	Units	Source
ρ [$(U_{1-y}Pu_y)O_2$]	$(10,970 + 490y)\,(a + bT + cT^2 + dT^3)^{-3}$, with $\left.\begin{matrix} a = 0.99734,\ b = 9.802 \times 10^{-6}, \\ c = -2.705 \times 10^{-10},\ d = 4.391 \times 10^{-13} \end{matrix}\right\}$, for $T \leqslant 923$ K, $\left.\begin{matrix} a = 0.99672,\ b = 1.179 \times 10^{-5}, \\ c = -2.429 \times 10^{-9},\ d = 1.219 \times 10^{-12} \end{matrix}\right\}$, for $T > 923$ K.	kg/m^3	[25,21]
α_T [$(U, Pu)O_{2-x}$]	$(a + bT + cT^2 + dT^3)(1 - 3.98x)$, with $\left.\begin{matrix} a = 9.828 \times 10^{-6},\ b = -6.390 \times 10^{-10}, \\ c = 1.33 \times 10^{-12},\ d = -1.757 \times 10^{-17} \end{matrix}\right\}$, for $T \leqslant 923$ K, $\left.\begin{matrix} a = 1.1833 \times 10^{-5},\ b = -5.013 \times 10^{-9}, \\ c = 3.756 \times 10^{-12},\ d = -6.125 \times 10^{-17} \end{matrix}\right\}$, for $T > 923$ K.	m/(m K)	[25,21]
E [$(U_{1-y}Pu_y)O_{2-x}$]	$2.334 \times 10^{11}\,(1 - 1.095 \times 10^{-4}\,T)\,(1 + 0.15y)\,\exp(-1.75x)$	Pa	[22]
ν [$(U, Pu)O_2$]	0.276		[22]
Q^* [$(U_{1-y}Pu_y)O_{2-x}$]	$-2.162 \times 10^5 \exp(-9.7x/y)$, with $x \leqslant 2y$	J/mol	[23,14]
F [$(U, Pu)O_2$]	1		[23,14]
D [$(U, Pu)O_2$]	$10^{-3.52-3.13\times10^3/T}$	m^2/s	[26]

in the UO_2 simulations presented here are consistent with the hyper-stoichiometric heat of transport data of Sari and Schumacher [14] and the thermodynamic factor, $F = 1$. The heat of transport for $(U_{1-y}Pu_y)O_{2-x}$ is given in terms of the ratio x/y and has the generic form

$$Q^*(x,y) \;=\; Q_0^* \;\exp\left(-\beta\,\frac{x}{y}\right). \tag{3.6}$$

The values of Q_0^* and β are given in Table 4, and the ratio x/y is related to the effective Pu valency, V_{Pu}, in $(U_{1-y}Pu_y)O_{2-x}$ by

$$V_{\text{Pu}} \;=\; 4 - 2\,\frac{x}{y}. \tag{3.7}$$

The data reported by Sari and Schumacher [14] cover the range, $3.2 < V_{\text{Pu}} \leqslant 4$. Therefore, the Pu content, y, and the deviation from stoichiometry, x, in Eq. (3.6) are not independent from each other, but must satisfy the condition

$$x \;<\; 0.4\,y. \tag{3.8}$$

In order to understand the interplay between the heat transport and the oxygen diffusion in the oxide fuel, it is useful to calculate the Lewis number for $(U_{1-y}Pu_y)O_{2-x}$ and compare with the Lewis number for UO_{2+x}. This comparison is illustrated in Fig. 5. The Lewis number, Le, is given by the ratio of the thermal diffusivity,

$$\alpha_{\text{th}} \;=\; \frac{k}{\rho\,C_P}, \tag{3.9}$$

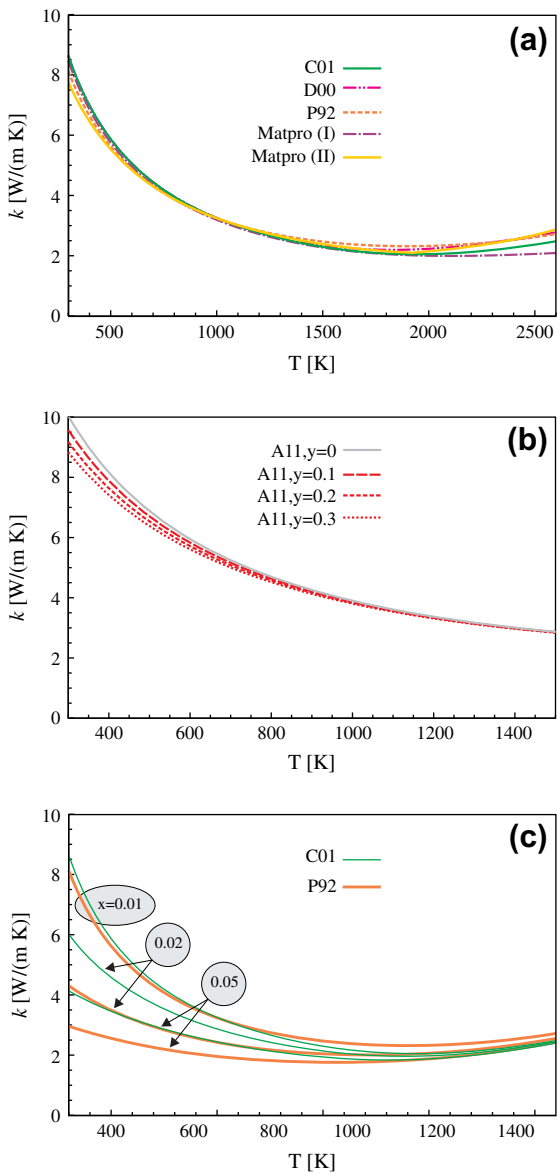

Fig. 2. Temperature dependence of the $(U,Pu)O_{2-x}$ thermal conductivity models considered in this paper. (a) Comparison of thermal conductivity models of stoichiometric (U, Pu)O_2. (b) Variability of the (U, Pu)O_2 thermal conductivity as a function of the Pu content, y, as inferred from the A11 model. (c) Stoichiometry dependence of the thermal conductivity models for $(U,Pu)O_{2-x}$, based on the C01 and P92 models. We note that in the temperature range $T < 1500$ K relevant for our simulations, where the models C01, D00 and MATPRO (I) are similar.

and the chemical diffusivity of the oxygen, D. We have

$$Le = \alpha_{th}/D. \tag{3.10}$$

The characteristic length scale in our problem is the radius of fuel pellet, R_{fuel}. Then, the characteristic time scale for heat diffusion is R^2_{fuel}/α_{th}, whereas the characteristic time scale for oxygen diffusion is R^2_{fuel}/D. Hence, the Lewis number is given by the ratio of the time required by the x spatial distribution to reach a steady state to the time required for by the T field to reach a steady state. The Lewis numbers for $(U_{1-y}Pu_y)O_{2-x}$ and UO_{2+x} depicted in Fig. 5 where computed using the C01 model for the $(U,Pu)O_{2-x}$ thermal conductivity and the UO_{2+x} thermal conductivity proposed by Amaya and collaborators [34], respectively. We find that the Lewis number for $(U,Pu)O_{2-x}$ is about four orders of magnitude smaller than the Lewis for UO_{2+x}. Therefore, we expect that the equilibration of the stoichiometry distribution in $(U,Pu)O_{2-x}$ occurs much faster than the equilibration of the stoichiometry distribution in UO_{2+x}. For most of the stoichiometry-temperature phase space, the Lewis number in $(U_{1-y}Pu_y)O_{2-x}$ is greater than 1, and therefore the oxygen diffusion lags behind the heat transport in $(U,Pu)O_{2-x}$. This result is insensitive to the Pu content and plays an important role in the transient behavior of the fuel under sudden changes in the operating conditions.

4. Results and discussion

Solutions of the coupled multi-physics problem in the fuel, gap and cladding are obtained by solving the heat transport Eq. (2.1) for the temperature, T, profile in the fuel, helium gap and zircaloy cladding, together with the oxygen diffusion characterized by the deviation from stoichiometry, x, given by Eqs. 2.6, 2.7, and 2.8, within the fuel. The fuel pellet and cladding are allowed to expand freely in the radial direction at the expense of the gap. A moving mesh application in the Lagrangian–Eulerian formulation is applied in the model to account for the changing gap size with thermal expansion of the fuel and the clad. The heat transport in the gap assumes that the helium in the gap is in perfect contact with both the fuel pellet and the cladding.

We perform simulations using the commercial finite-element code COMSOL Multiphysics. We calculate the heat transport using the heat-transport by conduction component of the Heat Transfer Module in COMSOL. The thermal deformation was calculated using the plane strain component of the Structural Mechanics Module in static or transient regime, as appropriate. Symmetric boundary conditions for solid mechanics, T, and x were applied along the straight edges of the fuel element. The numerical solutions of the coupled multi-physics problem were obtained using the linear solver in the default non-symmetric multi-frontal formulation (UMFPACK) in COMSOL. The finite-elements mesh uses quadratic Lagrange elements and we verified that numerical results converged with respect to the mesh-size distribution.

4.1. Steady-state simulations

In the case of steady-state simulations, the left-hand sides of Eqs. (2.1) and (2.3) are equal to zero. Hence, the flux of oxygen atoms vanishes ($J = 0$) everywhere in the fuel pellet and the steady-state solution is independent of the oxygen diffusivity.

Because Q^* in Eq. (3.6) is a function of both x and y, the Soret effect in (U, Pu)O_2 fuels is dependent on both x and y. So, the deviation from stoichiometry profile will change for different Pu contents in the fuel pellet, even though the Dirichlet boundary condition at the outer surface of the pellet does not change. This situation is illustrated in Fig. 6. The temperature decreases with increasing radius and the temperature values in the fuel pellet are much larger in magnitude than the temperatures observed in the cladding. Correspondingly, the thermal expansion is much larger in the pellet compared to the cladding. As such, in the following we will focus on the thermo-mechanical response in the fuel pellet. Profiles of temperature, radial displacement and deviations from stoichiometry will be depicted as a function the reduced radial position, r/R_{fuel}.

In Figs. 7 and 8, we show results of steady-state simulations performed using the (U, Pu)O_2 thermal conductivity models summarized in Table 5 and two values of the heat-generation rate, $Q = 2 \times 10^7$ W/m^3 and $Q = 2 \times 10^8$ W/m^3, respectively. All simulations correspond to a fixed temperature value, $T_b = 750$ K, at the outer surface of the cladding, and different fixed values of the deviations from stoichiometry at the surface of the pellet, x_b.

Table 5
Summary of thermal conductivity material models. Here we use the notation $t = T/1000$, with T measured in K.

Model (material)	Porosity	Functional form of the thermal conductivity	Units	Source
A11 $[(U_{1-y}Pu_y)O_2]$	0.035	$\lambda_0(t)\tan^{-1}[\theta(t,y)]/\theta(t,y) + 0.0595\,t^3$, with	W/(m K)	[29]
		$\lambda_0(t) = [0.0308 + 0.2294\,t]^{-1}$,	W/(m K)	
		$\theta(t,y) = \sqrt{D_{Pu}\,y\,\lambda_0(t)}$,		
		$D_{Pu} = 0.209\exp(1.09\,t)$.	m K/W	
C01 $[(U_{1-y}Pu_y)O_{2-x}]$	0.050	$[A(x) + C(x)t]^{-1} + 6400\,t^{-5/2}\exp(-16.35/t)$, with	W/(m K)	[25]
		$A(x) = 0.035 + 2.85x$,	m K/W	
		$C(x) = 0.286 - 0.715x$.	m/W	
		$[A(x) + C(x)t]^{-1} + 1689\,t^{-2}\exp(-13.52/t)$, with	W/(m K)	[30]
		$A(x) = 0.035 + 2.85x$,	m K/W	
		$C(x) = 0.286 - 0.715x$.	m/W	
P92 $[(U_{1-y}Pu_y)O_{2-x}]$	0.050	$[A(x) + C(x)t]^{-1} + 0.07638\,t^3$, with	W/(m K)	[31]
		$A(x) = 1.528\sqrt{x + 0.00931} - 0.1055$,	m K/W	
		$C(x) = 0.2885$.	m/W	
MATPRO (I) $[(U_{1-y}Pu_y)O_{2-x}]$	0.050	$[A(x) + C(x)t]^{-1} + 1500\,t^{-2}\exp(-13.52/t)$, with	W/(m K)	[22]
		$A(x) = 0.035 + 2.85x$,	m K/W	
		$C(x) = 0.286 - 0.715x$.	m/W	
MATPRO (II) $[(U_{1-y}Pu_y)O_2]$	0.050	$[A + C\tau_m]^{-1} + 0.0132\exp(1.88\,\tau)$, with	W/(m K)	[22]
		$A = 0.124783$,	m K/W	
		$C = 0.269022$,	m/W	
		and $\tau = T - 273.15$, $\tau_m = \min(\tau, 1650)$.	K	

Table 6
Summary of heat capacity material models.

Property (material)	Functional form of the property on temperature, T, and non-stoichiometry, x	Units	Source
C_P $[O_2]$	$b_0 + b_1T - b_{-2}T^{-2}$, with	J/(mol K)	[33]
	$b_0 = 195.96$,	J/(mol K)	
	$b_1 = 28.98 \times 10^{-3}$,	J/(mol K^2)	
	$b_{-2} = 2.018 \times 10^6$,	J K/mol	
C_P $[UO_2]$	$C_1(\theta/T)^2\frac{\exp(\theta/T)}{[\exp(\theta/T)-1]^2} + 2C_2T + C_3(E_a/T^2)\exp(-E_a/T)$, with	J/(mol K)	[20,32]
	$C_1 = 81.613$,	J/(mol K)	
	$C_2 = 2.285 \times 10^{-3}$,	J/(mol K^2)	
	$C_3 = 2.36 \times 10^7$,	J/mol	
	$\theta = 548.68$, $E_a = 18531.7$	K	
$C_P[PuO_2]$	$C_1(\theta/T)^2\frac{\exp(\theta/T)}{[\exp(\theta/T)-1]^2} + 2C_2T$, with	J/(mol K)	[25,32]
	$C_1 = 87.394$,	J/(mol K)	
	$C_2 = 3.978 \times 10^{-3}$,	J/(mol K^2)	
	$\theta = 587.41$	K	

The left hand-side panels in Figs. 7 and 8 illustrate the sensitivity of the steady-state results for $(U_{1-y}Pu_y)O_2$ with respect to the Pu content of the fuel pellet, y, as predicted by the A11 thermal conductivity model that includes an explicit dependence on y. The results corresponding to the C01 thermal conductivity model are included for comparison purposes, with the C01 model being independent of y. We find that the variability in the temperature and the deformation profiles due to the differences between the A11 and C01 models are slightly larger than the variability of these results with respect to the Pu content, y, in the A11 model. For a change in Pu content between 0% and 20%, the A11 model predicts changes of 2.7 K and 34 K in the centerline temperature, corresponding to a heat-generation rate values $Q = 2 \times 10^7$ W/m^3 and $Q = 2 \times 10^8$ W/m^3, respectively. For the same values of the heat-generation rates, Q, we find differences of 3.4 K and 64 K between the C01 and A11 model predictions.

In the right-sides panels of Figs. 7 and 8, we illustrate the sensitivity of the steady-state results in $(U,Pu)O_{2-x}$ fuel elements with respect to the deviation from stoichiometry, x. Here we compare results corresponding to the C01 and D92 thermal conductivity models for $y = 0.1$ and $y = 0.2$, respectively. We recall that the model for the heat of transport $Q^*(x,y)$ requires that the deviation from stoichiometry obeys the constraint given in Eq. (3.8). Therefore, the C01 and D92 are applied to different sets of values of the x_b boundary condition for the oxygen diffusion equation. We find large changes in the temperature and the deformation profiles corresponding to changes in x_b. Based on the D92 thermal conductivity model (appropriate for a 20% Pu content), in the non-stoichiometry interval 0.01–0.1, we find changes of 23 K and 140 K in the centerline temperature corresponding to the heat-generation rates, $Q = 2 \times 10^7$ W/m^3 and $Q = 2 \times 10^8$ W/m^3, respectively. By comparison, the predictions of the C01 $(y = 0.1)$ and D92 $(y = 0.2)$ models for $x_b = 0.01$ indicate changes of 6 K and 138 K in the centerline temperatures corresponding to the Q values considered in Figs. 7 and 8. Therefore, the results are more sensitive to x at small values of y. For larger values of y, the effects due to the deviation from stoichiometry and the Pu content are equally important.

4.2. Time-dependent simulations

In the spirit of our previous studies of thermo-mechanical simulations coupled with oxygen diffusion in oxide fuels [11–13], we consider three types of transient simulations. In the first two scenarios, the transient is driven by a rapid change (within 10 min) in the heat-generation rate, Q, according to the equation

$$Q(t) = Q_0 + \frac{Q_{max} - Q_0}{1 + 10\exp[-(-10 + t/\tau)]}, \tag{3.11}$$

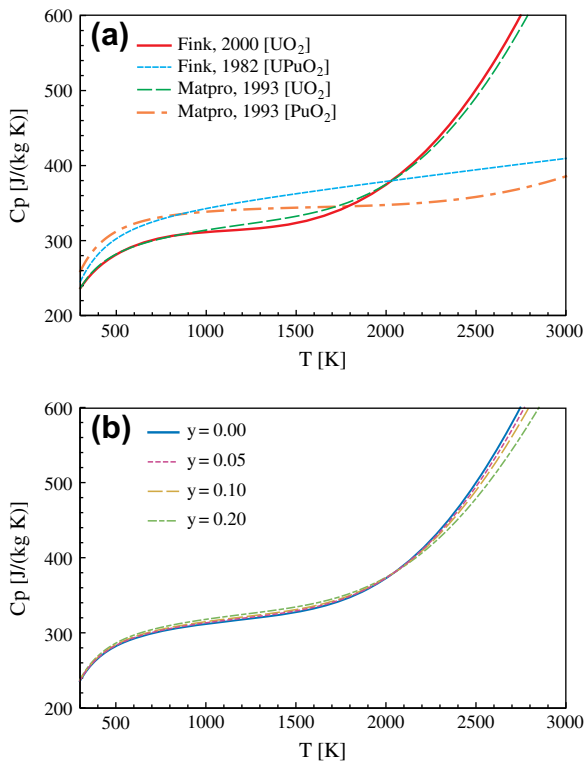

Fig. 3. Temperature dependence of heat capacity correlations used in this paper. (a) Heat capacity models for UO_2 and PuO_2 used to obtain the heat capacity for $(U,Pu)O_{2-x}$. (b) Variability of the $(U, Pu)O_2$ heat capacity as a function of the Pu content, y, as inferred from Eq. (3.3).

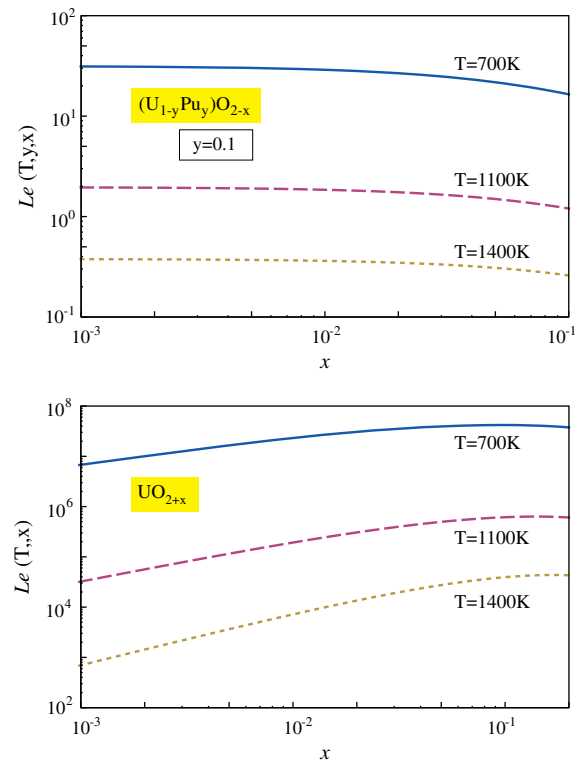

Fig. 5. Deviation from stoichiometry, x, dependence of the Lewis number, $Le = \alpha_{th}/D$, for several temperatures, $T = 800$ K, $T = 1100$ K, $T = 1200$ K. (a) Lewis number for a $(U_{1-y}Pu_y)O_{2-x}$ fuel with 10% Pu content, using the C01 model of the fuel thermal conductivity. (b) Lewis number for UO_{2+x}, using the models described in Refs. [11,12].

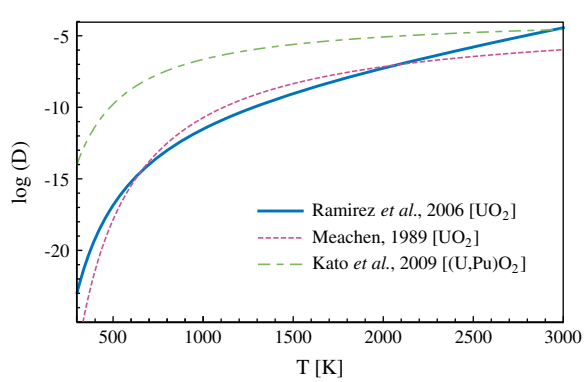

Fig. 4. Temperature dependence of oxygen chemical diffusion correlations for UO_2 and $(U, Pu)O_2$.

where Q_0 and Q_{max} are the initial and final values of the Q, respectively, and $\tau = 45$ s is a time constant. In a third scenario, the transient follows a change in the value of boundary condition for the non-stoichiometry at the outer surface of the fuel pellet, x_b, according to the equation

$$x_b(t) = x_{b,0} + \frac{x_{b,\max} - x_{b,0}}{1 + 100\exp[-(-5 + t/\tau)]}, \tag{3.12}$$

where $x_{b,0}$ and $x_{b,\max}$ are the initial and final values of x_b, respectively. These scenarios are only intended to evaluate the sensitivity of the dynamical response of fuel element to the material models used in our simulations.

In Figs. 9 and 10 we depict the results corresponding to a start-up reactor scenario. In this case, the heat-generation rate varies from a zero initial value $Q_0 = 0$ to a final value $Q_{max} = 2 \times 10^8$ W/m^3, according to Eq. (3.11). Similarly, in Figs. 11 and 12 we show results corresponding to a time-dependent heat-generation scenario with the heat-generation rate varying from an initial value $Q_0 = 2 \times 10^7$ W/m^3 to a final value $Q_{max} = 2 \times 10^8$ W/m^3, according to Eq. (3.11). In both cases, the temperature at the outer surface of the cladding is fixed to the initial temperature, $T_b = 750$ K. We consider two non-stoichiometry Dirichlet boundary conditions, $x_b = 0.01$ and $x_b = 0.05$, respectively. The heat-generation scenarios depicted in Figs. 11 and 12 correspond to having the state of the fuel element transition between the $x_b = 0.01$ and $x_b = 0.05$ steady-state profiles, corresponding to heat-generation rates, $Q = 2 \times 10^7$ W/m^3 and $Q = 2 \times 10^8$ W/m^3, shown in Figs. 7 and 8, respectively. Hence, for the time-dependent heat-generation rate scenario, the initial condition is set by solving the steady-state problem for fuel pellet with $x_b = 0.01$ and $x_b = 0.05$, respectively, and the initial heat-generation rate, $Q_0 = 2 \times 10^7$ W/m^3.

As discussed earlier, the relative characteristic time scale of oxygen diffusion and heat transport is characterized by the Lewis number. For $(U,Pu)O_{2-x}$ fuels the Lewis number has values lower by several orders of magnitude compared to UO_{2+x} fuels. Therefore, even though the equilibration of the deviation from stoichiometry remains slower than the equilibration of the temperature profile, $Le > 1$, the equilibration of the x profile occurs much faster in $(U,Pu)O_{2-x}$ than UO_{2+x} fuels. As a consequence, in the $(U_{1-y}Pu_y)O_{2-x}$ simulations illustrated in Figs. 9–12 we do not observe the second transient response observed in similar simulations of UO_{2+x} fuels [11–13]. In UO_{2+x}, the equilibration of the

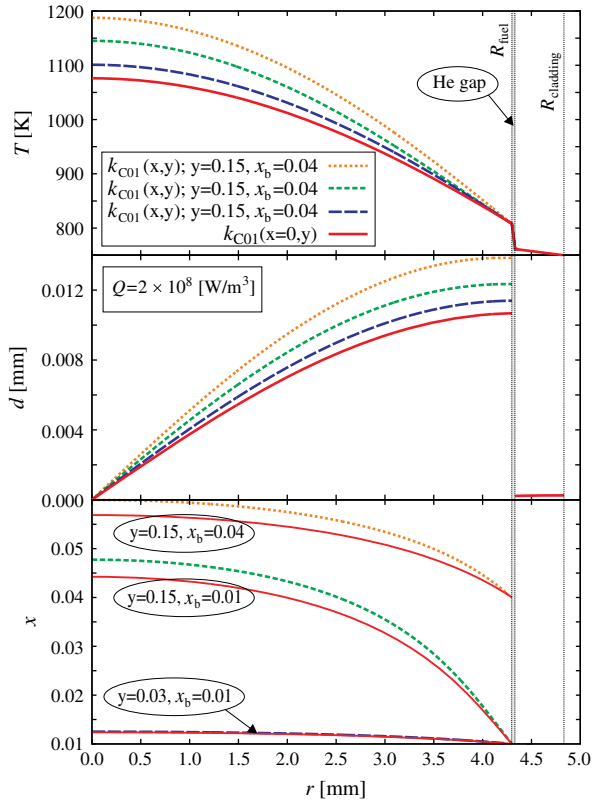

Fig. 6. Comparison of steady-state radial profiles of the temperature, T, total radial displacement, d, and deviation from stoichiometry, x, calculated with and without including the x dependence in the C01 model of the fuel thermal conductivity. Here, we consider a $(U_{1-y}Pu_y)O_{2-x}$ fuel element with a heat-generation rate, $Q = 2 \times 10^8$ W/m^3.

centerline deviation from stoichiometry, x_0, lags behind the evolution of the centerline temperature for $k(T, x)$ models as the characteristic time associated with oxygen diffusion is much larger than the heat transport characteristic time, and the second transient in the centerline temperature and the total displacement at the outer edge of the fuel pellet coincides with the centerline non-stoichiometry value reaching its equilibrium. This situation is reflected in part in Figs. 9–12 by the baseline A11 model simulations for $y = 0$, for which we note the delayed equilibration of the centerline deviation from stoichiometry relative to the equilibration of the centerline temperature. However, no secondary transient is found in the A11($y = 0$) simulations, because this thermal conductivity model is x independent and there is no coupling between heat transport and oxygen diffusion in this case. Therefore, for $(U_{1-y}Pu_y)O_{2-x}$ fuels, the time evolution of the centerline temperature, T_0, the radial total displacement at the surface of the pellet, $d(R_{fuel})$, and the centerline deviation from stoichiometry, x_0, closely track each other in response to a change in the heat-generation rate. It is noteworthy that the spread in the final state between the predictions of the various models considered here is 236 K and 305 K, corresponding to the two fixed boundary-condition values, $x_b = 0.01$ and $x_b = 0.05$, respectively. The spread of the A11 models is 34 K, whereas the difference between the C01 ($y = 0.1$) and D92 ($y = 0.2$) models is 138 K and 145 K, respectively. So, the results of these simulations depend strongly on both the deviation from stoichiometry, x, and the Pu content, y.

For completeness, in Fig. 13 we show the results from our third scenario simulations. In this scenario, the transient corresponds to a time-dependent non-stoichiometry Dirichlet boundary condition at the outer surface of the fuel pellet, x_b. In these simulations, we fix the temperature at the outer face of the cladding, $T_b = 750$ K, and the heat-generation rate has a constant value, $Q = 2 \times 10^8$ W/m^3. The non-stoichiometry at the outer face of the fuel pellet, x_b, changes according to Eq. (3.12) from an initial value

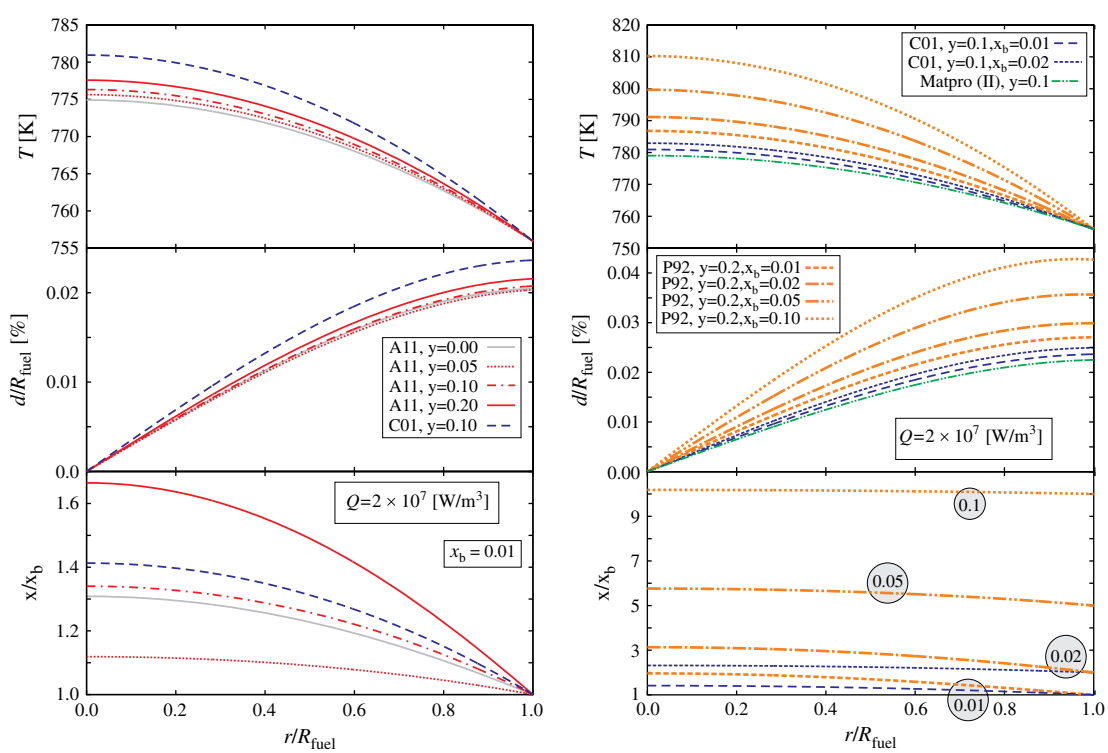

Fig. 7. Steady-state radial profiles of the temperature, T, total radial displacement, d, and deviation from stoichiometry, x, in the $(U, Pu)O_{2-x}$ fuel element for a heat-generation rate, $Q = 2 \times 10^7$ W/m^3. In these simulations we chose a temperature boundary condition, $T_b = 750$ K, and considered several values of the non-stoichiometry boundary condition, x_b.

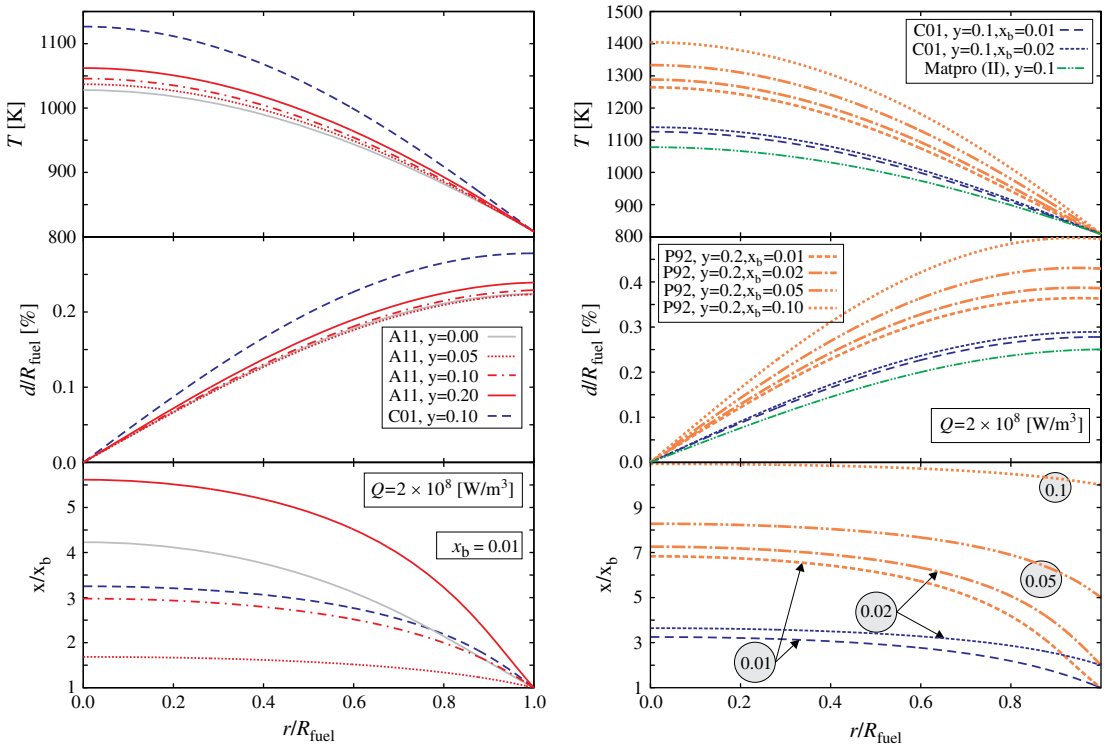

Fig. 8. Steady-state radial profiles of the temperature, total radial displacement and non-stoichiometry in the $(U,Pu)O_{2-x}$ fuel element for a heat-generation rate, $Q = 2 \times 10^8$ W/m^3. Here the temperature boundary condition is $T_b = 750$ K, and the non-stoichiometry boundary condition, x_b, is varied.

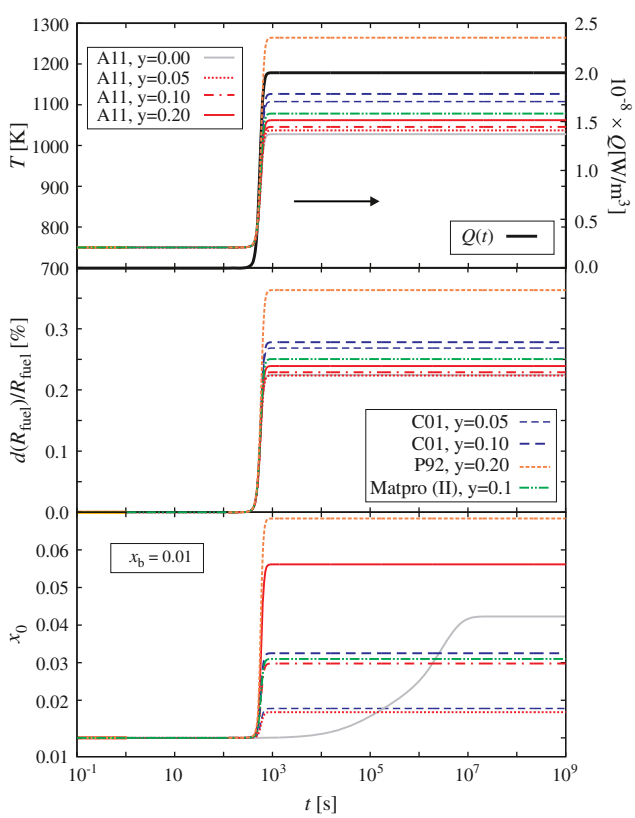

Fig. 9. Results of transient simulations for a start-up reactor scenario in the $(U,Pu)O_{2-x}$ fuel element. We illustrate the time evolution of the centerline temperature, T_0, total radial displacement of the outer surface of the fuel pellet, $d(R_{fuel})$, and centerline deviation from stoichiometry, x_0. The calculations are performed by imposing Dirichlet boundary conditions for temperature, $T_b = 750$ K, and composition, $x_b = 0.01$.

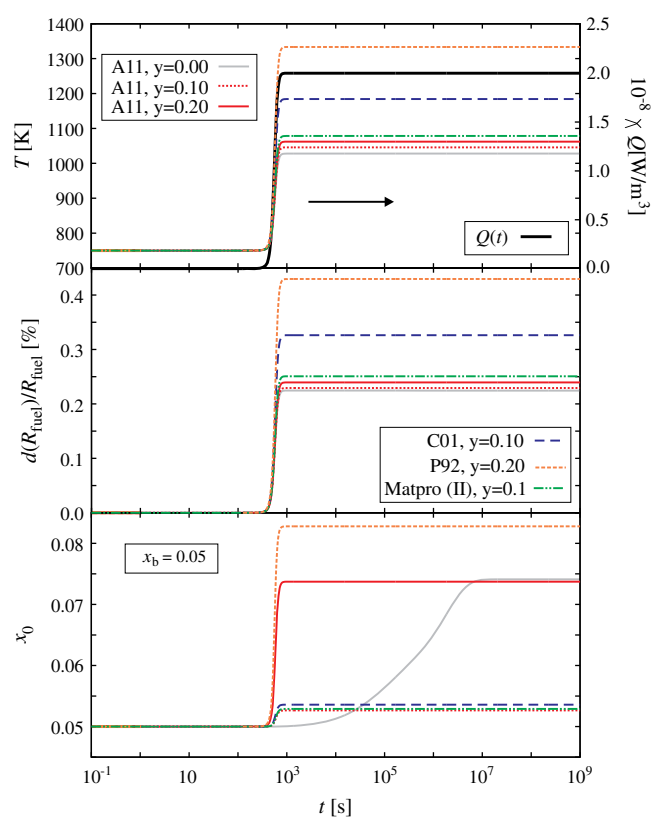

Fig. 10. Results of transient simulations for a start-up reactor scenario in the $(U,Pu)O_{2-x}$ fuel element. Here, we imposed Dirichlet boundary conditions for temperature, $T_b = 750$ K, and composition, $x_b = 0.05$.

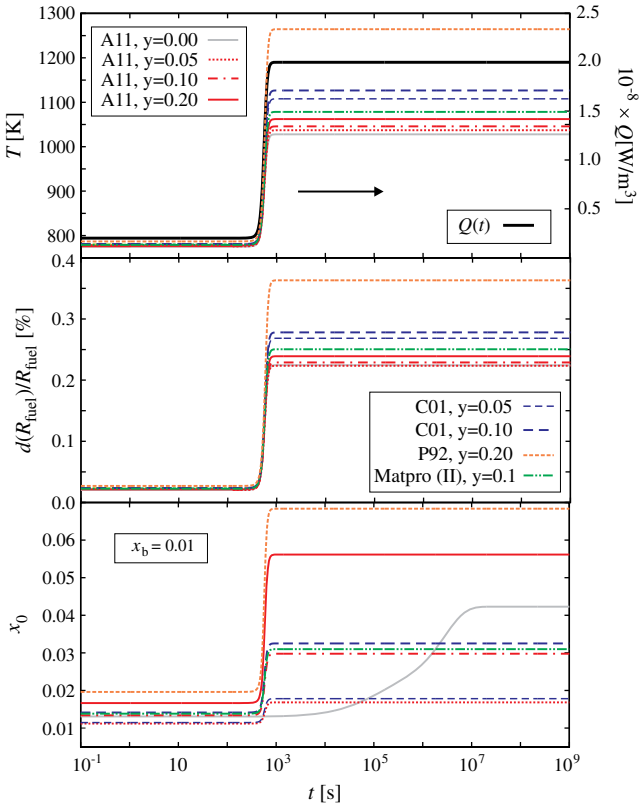

Fig. 11. Results of transient simulations for a heat-generation scenario in the $(U,Pu)O_{2-x}$ fuel element. Here, we imposed Dirichlet boundary conditions for temperature, $T_b = 750$ K, and composition, $x_b = 0.01$.

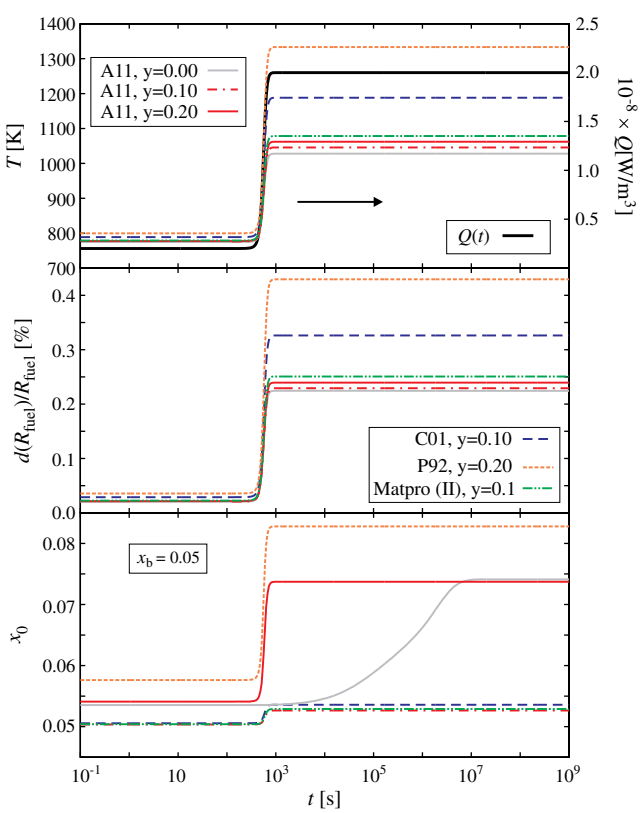

Fig. 12. Results of transient simulations for a heat-generation scenario in the $(U,Pu)O_{2-x}$ fuel element. Here, we imposed Dirichlet boundary conditions for temperature, $T_b = 750$ K, and composition, $x_b = 0.05$.

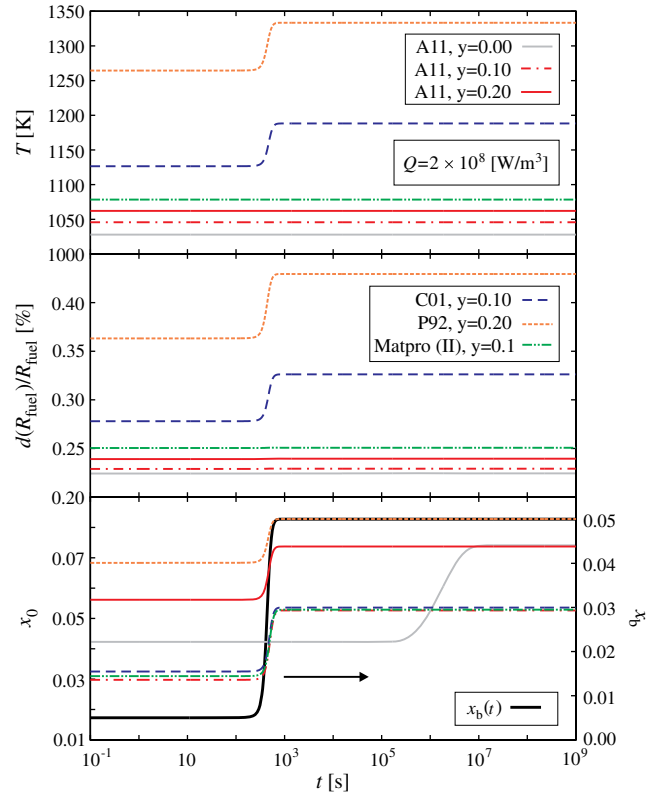

Fig. 13. Results of transient simulations for a time-dependent non-stoichiometry boundary conditions scenario in the $(U,Pu)O_{2-x}$ fuel element. Here we consider Dirichlet boundary conditions for temperature, $T_b = 750$ K, and a heat-generation rate, $Q = 2 \times 10^8$ W/m^3.

$x_{b,0} = 0.01$ to a final value $x_{b,max} = 0.05$ over the course of approximately 10 min. This scenario corresponds to having the state of the fuel element transition between the $x_b = 0.01$ and $x_b = 0.05$ profiles for $Q = 2 \times 10^8$ W/m^3, as shown in Fig. 8. Hence, for the time-dependent heat-generation rate scenario, the initial condition is set by solving the steady-state problem for fuel pellet with $x_b = 0.01$ and the heat-generation rate, $Q_0 = 2 \times 10^8$ W/m^3.

The time evolution of the total radial displacement due to thermal expansion follows the time evolution of the temperature, and the characteristic time scales of the heat transport and the oxygen diffusion in $(U,Pu)O_{2-x}$ are similar. Just like in the $Q(t)$ simulations discussed above, the time evolution of the centerline temperature, T_0, the radial total displacement at the surface of the pellet, $d(R_{fuel})$, and the centerline deviation from stoichiometry, x_0, closely track each other. The change in these observables follows closely the change in the deviation from stoichiometry at the outer surface of the fuel pellet, x_b. The results are sensitive to the thermal conductivity model employed with the thermo-mechanical response being greatly sensitive to both the Pu content, y, and the deviation from stoichiometry, x. The temperature and deformation profiles predicted by the A11 and Matpro (II) models are constant in time, because these thermal conductivity models do not depend on the deviation from stoichiometry and the oxygen diffusion does not impact their predictions. The change in the thermo-mechanical response predicted by the A11 model for the range of Pu compositions considered here is three times smaller than the change in response predicted by the C01 and P92 models for $y = 0.1$ and $y = 0.2$, respectively. Also, the centerline temperatures predicted by the A11 model are consistently smaller than those predicted by the C01 and P92 models, as the A11 thermal conductivity is smaller than C01 and P92 ones at low temperatures. The A11 predictions for large Pu content are consistent with the MATPRO (II) model predictions.

5. Conclusions

Although urania and plutonia are characterized by the same fluorite structure, plutonium oxides tend to be hypo-stoichiometric, PuO_{2-x}, whereas uranium oxides are most often hyper-stoichiometric, UO_{2+x}. For fuel-performance studies, it is important to understand the differences between the behavior of nuclear fuel materials such as UO_{2+x} and $(U_{1-y}Pu_y)O_{2-x}$ fuel elements as a function of the Pu content, y, and the deviation from stoichiometry, x. Therefore, in this paper we studied the impact of different thermal conductivity models on the thermal response and the radial fuel deformation of a generic $(U, Pu)O_2$ fuel element using multi-physics simulations of coupled thermal transport, oxygen diffusion, and thermal expansion. A series of steady-state and time-dependent finite-element simulations with a variety of initial-value conditions show that including the Pu content, y, and deviation from stoichiometry, x, in the thermal conductivity model, $k(T, y, x)$, results in significant changes in the evaluation of the centerline temperature T_0 and the extent of the radial deformation of the fuel pellet, compared with simulations that do not account for the oxygen or Pu content.

Our steady-state simulation results indicate that the radial temperature and deformation profiles are more sensitive to x for small values of y. For larger values of y, the effects due to the deviation from stoichiometry and the Pu content are equally important. In turn, our time-dependent simulations highlight the fact that in $(U_{1-y}Pu_y)O_{2-x}$ the characteristic time scales of the heat transport and oxygen diffusion are similar. Hence, the time evolution of the centerline temperature, T_0, the radial total displacement at the surface of the pellet, $d(R_{fuel})$, and the centerline deviation from stoichiometry, x_0, closely track each other, in response to a change in the heat-generation rate. This is in contrast with the case of UO_{2+x} fuels, where the equilibration of the centerline deviation from stoichiometry, x_0, lags behind the evolution of the centerline temperature for $k(T, x)$ models as the characteristic time associated with oxygen diffusion is much larger than the heat transport characteristic time. In UO_{2+x} this mechanism results in a second transient in the centerline temperature and the total displacement at the outer edge of the fuel pellet that coincides with the centerline non-stoichiometry value reaching its equilibrium value. The second transient is not observed in our $(U_{1-y}Pu_y)O_{2-x}$ fuel simulations.

We find that the centerline temperatures predicted by the A11 model are consistently smaller than those predicted by the C01 and P92 models, as the A11 thermal conductivity is smaller than C01 and P92 ones at low temperatures. This is important because the A11 model is the only thermal conductivity model available at this time that has an explicit Pu content dependence, whereas the C01 and P92 models are intended for low and large Pu content in $(U, Pu)O_{2-x}$. The differences in the thermal conductivity models may result in large differences in the predicted centerline temperature value and total displacement at the outer edge of the fuel pellet. For example, the uncertainty in the thermo-mechanical response due to the x- and y-dependence of the thermal conductivity models, results in differences of up to 236 K and 305 K in the predicted values of the centerline temperatures in the initial $(x_b = 0.01)$ and final $(x_b = 0.05)$ states, respectively, as seen in Fig. 13. These differences increase with the heat-generation rate and the non-stoichiometry boundary condition at the outer surface of the pellet.

Acknowledgments

This work was performed under the auspices of the United States Department of Energy. BM gratefully acknowledges partial financial support from the Consortium for Advanced Simulation of Light Water Reactors (www.casl.gov), an Energy Innovation Hub (http://www.energy.gov/hubs) for Modeling and Simulation of Nuclear Reactors under U.S. Department of Energy Contract No. DE-AC05-00OR22725. MS research is supported by the U.S. Department of Energy, Office of Science under Contract No. DE-AC02-06CH11357

References

[1] F. Ganda, E. Greenspan, Nucl. Eng. Des. 239 (2009) 1489.
[2] K. Maeda, S. Sasaki, M. Kato, Y. Kihara, J. Nucl. Mater. 385 (2009) 413.
[3] B.-H. Lee, Y.-H. Koo, J.-Y. Oh, J.-S. Cheon, D.-S. Sohn, Nucl. Technol. 157 (2007) 53.
[4] M.H.A. Piro, T.M. Besmann, S. Simunovic, B.J. Lewis, W.T. Thompson, J. Nucl. Mater. 414 (2011) 399–407.
[5] C. Gueneau, N. Dupin, B. Sundman, C. Martial, J.-C. Dumas, S. Gosse, S. Chatain, F. De Bruycker, D. Manara, R.J.M. Konings, J. Nucl. Mater. 419 (2011) 145.
[6] K. Morimoto, M. Kato, M. Ogasawara, M. Kashimura, J. Nucl. Mater. 389 (2009) 179.
[7] K. Morimoto, M. Kato, M. Ogasawara, M. Kashimura, J. Nucl. Mater. 374 (2008) 378.
[8] P.R.V. Rao, S. Anthonysamy, M.V. Krishnaiah, V. Chandramouli, J. Nucl. Mater. 348 (2006) 329.
[9] M. Stan, Nucl. Eng. Technol. 41 (2009) 39.
[10] M. Stan, Mater. Today 12 (2009) 20.
[11] J.C. Ramirez, M. Stan, P. Cristea, J. Nucl. Mat. 359 (2006) 174.
[12] B. Mihaila, M. Stan, J.C. Ramirez, A. Zubelewicz, P. Cristea, J. Nucl. Mat. 394 (2009) 182.
[13] B. Mihaila, M. Stan, J. Crapps, J. Nucl. Mat. 430 (2012) 221.
[14] C. Sari, G. Schumacher, J. Nucl. Mater. 61 (1976) 192.
[15] S.R. De Groot, Thermodynamics of Irreversible Processes, North Holland Publ. Co., Amsterdam, 1951.
[16] C. Korte, J. Janek, H. Timm, Solid State Ionics 101 (103) (1997) 465.
[17] C. Newman, G. Hansen, D. Gaston, J. Nucl. Mater. 392 (2009) 6.
[18] A. Bejan, Heat Transfer, first ed., John Wiley & Sons, New York, 1993.
[19] IAEA-TECDOC-1496, Thermophysical properties database of materials for light water reactors and heavy water reactors, IAEA, Vienna, 2006.
[20] J.K. Fink, J. Nucl. Mater. 279 (2000) 1.
[21] D.G. Martin, J. Nucl. Mater. 152 (1988) 94.
[22] D.T. Hagrman, editor, SCDAP/RELAP5/MOD3.1 code manual, Volume IV: MATPRO – a library of materials properties for light-water-reactor accident analysis, NUREG/CR-6150, EGG-2720. vol: IV; 1993.
[23] K. Lassmann, J. Nucl. Mater. 150 (1987) 10.
[24] J.A. Meachen, Nucl. Energy 28 (1989) 221.
[25] J.J. Carbajo, G.L. Yoder, S.G. Popov, V.K. Ivanov, J. Nucl. Mater. 299 (2001) 181.
[26] M. Kato, K. Morimoto, T. Tamura, T. Sunaoshi, K. Konashi, S. Aono, M. Kashimura, J. Nucl. Mater. 389 (2009) 416.
[27] P.G. Lucuta, Hj. Matzke, I.L. Hastings, J. Nucl. Mater. 232 (1996) 166.
[28] C. Ronchi, M. Sheindlin, M. Musella, G.J. Hyland, J. Appl. Phys. 85 (1999) 776.
[29] M. Amaya, J. Nakamura, F. Nagase, T. Fuketa, J. Nucl. Mat. 414 (2011) 303.
[30] C. Duriez, J.P. Alessandri, T. Gervais, Y. Philipponneau, J. Nucl. Mater. 277 (2000) 143.
[31] Y. Philipponneau, J. Nucl. Mater. 188 (1992) 194.
[32] J.K. Fink, Int. J. Thermophys. 3 (1982) 165.
[33] J.D. Higgs, B.J. Lewis, W.T. Thompson, D.M. Thompson, Z. He, J. Nucl. Mater. 366 (2007) 99.
[34] M. Amaya, T. Kubo, Y. Korei, J. Nucl. Sci. Technol. 33 (1996) 636.